# Three-dimensional convection of binary mixtures in porous media

R. Umla,* M. Augustin, B. Huke, and M. Lücke
*Institut für Theoretische Physik, Universität des Saarlandes, Postfach 151150, D-66041 Saarbrücken, Germany*
(Received 8 April 2011; revised manuscript received 28 October 2011; published 28 November 2011)

We investigate convection patterns of binary mixtures with a positive separation ratio in porous media. As setup, we choose the Rayleigh-Bénard system of a fluid layer heated from below. Results are obtained by a multimode Galerkin method. Using this method, we compute square and crossroll patterns, and we analyze their structural, bifurcation, and stability properties. Evidence is provided that, for a strong enough Soret effect, both structures exist as stable forms of convection. Some of their properties are found to be similar to square and crossroll convection in the system without porous medium. However, there are also qualitative differences. For example, squares can be destabilized by oscillatory perturbations with square symmetry in porous media, and their velocity isolines are deformed in the so-called Soret regime.

DOI: 10.1103/PhysRevE.84.056326 PACS number(s): 47.56.+r, 47.20.Bp, 47.54.−r

## I. INTRODUCTION

A popular setup to investigate convection and pattern formation of fluids in porous media is the Rayleigh-Bénard system. It consists of two horizontal parallel plates, say, in the earth's gravitational field. They confine a porous medium that is entirely saturated with a fluid. To obtain convection patterns, a temperature gradient is applied between the plates. The lower plate is adjusted to a higher temperature than the upper one. This gives rise to density differences and hence to buoyancy in the presence of gravity. When the temperature difference exceeds a critical value, convection in the form of rolls emerges in the simple case of a pure, i.e., one-component fluid saturating the porous medium. This form of convection is described in the literature as Bénard rolls, ideal straight rolls, or steady overtuning convection. Important aspects of the Bénard rolls like their stability and heat transport have been investigated theoretically, for example, in Refs. [1,2] as well as experimentally in Refs. [3,4].

Since in many natural processes and applications the fluid has to be treated as a binary mixture consisting of two fluid components rather than only one (see, e.g., Ref. [5]), it is also of interest to investigate Bénard rolls for binary fluids as has been done in Refs. [6,7]. In binary mixtures, the concentration field changes the spatiotemporal properties of convection because concentration differences lead to density gradients and thus contribute to the buoyancy. This change becomes crucial if the so-called Soret effect is observed in the mixture, i.e., if concentration currents are driven by thermal gradients. Whereas advection and diffusion tend to equilibrate concentration gradients, the Soret effect sustains concentration differences being relevant for the structure and the dynamics of convection. The present authors have investigated mixtures with a positive Soret effect that saturate a porous medium [6]. Therein the heavier component is driven into the direction of lower temperatures. That in turn destabilizes the conductive ground state and leads to a lower convective threshold. As a main result, Bénard rolls have been found to loose their stability at the onset of convection for a strong enough positive Soret effect.

A similar situation is known for the classical Rayleigh-Bénard system without porous medium. In this so-called clear fluid system, it has been found that when rolls lose their stability at onset due to a positive Soret effect, they are replaced by a three-dimensional square pattern. When the thermal driving is increased, this square pattern is transformed again into rolls. This transition occurs smoothly via so-called crossrolls. For research in this field, we refer to the experimental studies in Refs. [8,9], wherein squares are analyzed by using shadowgraph as well as heat-transport measurements, and to the theoretical studies in Refs. [10,11], which investigate fixed-point solutions as well as stability properties of squares and crossrolls.

However, in the Rayleigh-Bénard setup with a porous medium, it was unknown so far whether squares and crossrolls exist in this system. The aim of our paper is to close this gap, i.e., to provide evidence for the existence of squares and crossrolls in the porous medium system and to describe their structural, bifurcation, and stability properties.

Our paper is organized as follows: In Sec. II we introduce the underlying equations of the system and the Galerkin method that we have used for our numerical computations. In Sec. III we discuss the bifurcation scenario of rolls, squares, and crossrolls. We give results for Nusselt and mixing numbers, and we analyze the structure of the fields of velocity, temperature, and concentration of square convection. In Sec. IV the results of a restricted stability analysis are presented. It takes into account only perturbations that have the same lateral periodicity as the underlying pattern. In particular, our analysis reveals a new instability mechanism that is not known in the clear fluid system. The conclusion is given in Sec. V.

## II. FOUNDATIONS

### A. System and basic equations

Here we give only a brief summary of the system and the governing equations. For more details see Ref. [6]. We consider two infinite horizontal parallel plates perpendicular to a homogeneous gravitational field in $z$ direction. The lower plate is positioned at $z = -1/2$, the upper one at $z = 1/2$. Both plates are impermeable and ideally heat conducting.

*rudolf@lusi.uni-sb.de

 

The temperature at the plates is fixed. The space between the plates is filled with a porous medium that is considered to be isotropic and homogeneous. The porous medium is saturated with a binary fluid mixture. Moreover, we assume local thermal equilibrium between the fluid and the porous medium such that there is no heat transfer between both phases (for literature which investigates when this assumption is reasonable, we refer the reader to Ref. [12]).

We use the following nondimensional balance equations:

$$\nabla \cdot \boldsymbol{u} = 0, \tag{2.1a}$$

$$\gamma_a \partial_t \boldsymbol{u} = -\nabla p - \boldsymbol{u} + (\theta + c)\boldsymbol{e}_z, \tag{2.1b}$$

$$\partial_t \theta + (\boldsymbol{u} \cdot \nabla)\theta = Rw + \nabla^2 \theta, \tag{2.1c}$$

$$\phi^* \partial_t c + (\boldsymbol{u} \cdot \nabla)c = R\psi w + L(\nabla^2 c - \psi \nabla^2 \theta), \tag{2.1d}$$

assuming the Oberbeck-Boussinesq approximation is valid. Here convection is described by the Darcy velocity $\boldsymbol{u} = (u,v,w)$, the deviation $\theta$ of the temperature field $T$ from its linear conductive ground-state profile $T_{\text{cond}}$, the deviation $c$ of the concentration field $C$ from its linear ground-state profile $C_{\text{cond}}$, and the pressure deviation $p$. In the conductive ground state one has

$$\boldsymbol{u}_{\text{cond}} = 0, \quad T_{\text{cond}}(z) = T_0 - Rz, \quad C_{\text{cond}}(z) = C_0 + R\psi z, \tag{2.2}$$

where the index 0 denotes the spatial average of the fields.

Parameters are the Lewis number $L$, which is the quotient of solutal and thermal diffusion times, the Rayleigh-Darcy number $R$, which measures the temperature difference between the plates, and the separation ratio $\psi$, which measures the strength and direction of the Soret effect. The parameters $\gamma_a$ and $\phi^*$ are specific for the system with a porous medium. Note, however, that the stationary solutions of Eqs. (2.1) do not depend on $\gamma_a$ and $\phi^*$. $\gamma_a$ consists of the ratio of the timescale corresponding to the friction term $-\mathbf{u}$ and the temperature diffusion time of the whole medium multiplied by a correction factor, which is needed for the sake of consistency between a description by the Darcy equation and experimental results [13].

$\gamma_a$ is usually very small, and its exact value has therefore no relevant influence on the dynamics. It is fixed to 0.0001 for all calculations presented in this paper. Changes for even smaller $\gamma_a$ turned out to be negligible. The normalized porosity $\phi^*$ is the product of the porosity and the ratio of the heat capacities of the fluid and the whole system. Multiplying the time derivative of concentration in Eq. (2.1d), $\phi^*$ sets the time scales for changes in $c$ relative to those in $\theta$. $\phi^*$ falls between 0 and 1.

For the reader's convenience, we list the definitions of the system parameters:

$$R = \frac{\rho_0 g \beta_T K C_f d}{\lambda_{\text{tot}} \eta} \Delta T, \quad \psi = -\frac{\beta_C}{\beta_T}\frac{k_T}{T_0}, \tag{2.3}$$

$$L = \frac{D_{\text{tot}} \phi C_f}{\lambda_{\text{tot}}}, \quad \phi^* = \frac{C_f}{C_{\text{tot}}}\phi, \quad \gamma_a = \frac{K \lambda_{\text{tot}} \eta}{d^2 C_{\text{tot}} \rho_0} c_a. \tag{2.4}$$

Here $\rho_0$ is the mean density of the fluid, $T_0$ the mean temperature, $\eta$ the dynamic viscosity, $\beta_T$ ($\beta_C$) the thermal (solutal) expansion coefficient of the fluid, and $K$ the permeability of the porous medium. $C_f$,$C_s$, and $C_{\text{tot}}$ denote the heat capacity per unit volume of the fluid, of the solid matrix, and of the total medium (fluid and solid matrix), respectively. The heat capacities per unit volume can be connected via the porosity $\phi$ of the porous medium by the relation $C_{\text{tot}} = \phi C_f + (1-\phi)C_s$. The same holds true for the thermal conductivities $\lambda_f$, $\lambda_s$, and $\lambda_{\text{tot}}$. $D_{\text{tot}}$ is the concentration diffusivity of the total medium, which is equal to $\phi D$, and $D$ is the concentration diffusivity of the fluid. $k_T$ is the thermodiffusion ratio, which characterizes the strength of the Soret effect. The correction factor $c_a$ brings the Darcy equation in agreement with experimental results (see Ref. [13]). $d$ is the distance between the plates, $g$ the gravitational constant, and $\Delta T$ the temperature difference between the plates.

We assume impermeable and ideal heat conducting plates, which imply the boundary conditions

$$w = \theta = \partial_z(c - \psi\theta) = 0 \quad \text{at} \quad z = \pm\tfrac{1}{2}. \tag{2.5}$$

In order to get independent boundary conditions for each field, we use the field

$$\zeta = c - \psi\theta \tag{2.6}$$

as in the clear fluid case. The corresponding balance equation for $\zeta$ can directly be derived by combining Eqs. (2.1c) and (2.1d).

Additionally, one can simplify the numerical treatment of Eq. (2.1b) by introducing two scalar potentials $\Phi$ and $\Psi$ such that $\boldsymbol{u}$ can be written as

$$\boldsymbol{u} = \nabla \times \nabla \times (\Phi \boldsymbol{e}_z) + \nabla \times (\Psi \boldsymbol{e}_z), \tag{2.7}$$

which is possible because of the incompressibility condition Eq. (2.1a). Equations for $\Phi$ and $\Psi$ can be derived by applying the curl to the momentum balance Eq. (2.1b) once or twice and taking the $z$ component in both cases. This yields

$$\gamma_a \partial_t \Delta_{xy} \Psi = -\Delta_{xy} \Psi, \tag{2.8a}$$

$$\gamma_a \partial_t \nabla^2 \Delta_{xy} \Phi = -\nabla^2 \Delta_{xy} \Phi - \Delta_{xy}(\theta + c), \tag{2.8b}$$

with $\Delta_{xy} = \partial_x^2 + \partial_y^2$. Note that these equations do not contain any pressure term. One can choose $\Psi \equiv 0$ and neglect Eq. (2.8a) as long as no transient behavior is investigated and there is no mean flow in the system [6]. The boundary condition on $\boldsymbol{u}$ implies

$$\Phi = 0 \quad \text{at} \quad z = \pm\tfrac{1}{2}. \tag{2.9}$$

### B. Numerical method

To describe convection patterns, we used a Galerkin method with the following ansatz for the fields:

$$X(x,y,z) = \sum_{l}^{N_l} \sum_{m}^{N_m} \sum_{n}^{N_n} X_{lmn} \cos(lkx) \cos(mky) f_n(z), \tag{2.10}$$

$X = \Phi, \theta, \zeta$, which is motivated by similar work on the Rayleigh-Bénard system without porous medium [11,14,15]. $k$ is the lateral wave number, and the $f_n(z)$ are an orthogonal

set of trigonometric functions that each fulfill the boundary conditions at the plates. We choose

$$\text{for } \Phi, \quad \theta : f_n(z) = \begin{cases} \sqrt{2}\cos(n\pi z) & \text{if } n = 1,3,5,\ldots \\ \sqrt{2}\sin(n\pi z) & \text{if } n = 2,4,6,\ldots \end{cases} \tag{2.11}$$

$$\text{for } \zeta : f_n(z) = \begin{cases} \sqrt{2}\sin(n\pi z) & \text{if } n = 1,3,5,\ldots \\ \sqrt{2}\cos(n\pi z) & \text{if } n = 2,4,6,\ldots \\ 1 & \text{if } n = 0. \end{cases} \tag{2.12}$$

The lateral index $m$ starts from 0 for $\theta$ and $\zeta$ and from 1 for $\Phi$. All $\theta$ and $\zeta$ modes with $n+m > N$ and all $\Phi$ modes with $n+m > N/2$ are neglected, where we choose $N = 24$ if not otherwise specified. The fact that our truncation keeps fewer modes in $\Phi$ than in $\theta$ and in $\zeta$ is motivated by Ref. [16].

In addition to their symmetry in the $x$ and $y$ direction, the structures under consideration fulfill the so-called mirror-glide symmetry [11]:

$$X(x,y,z) = -X\left(x+\frac{\pi}{k}, y+\frac{\pi}{k}, -z\right). \tag{2.13}$$

As a consequence, we can set one half of the modes to zero. Then, we insert the ansatz into the basic equations and project onto the ansatz functions, which yields a coupled system of nonlinear equations. This set of equations is solved for fixed points by a Newton-Raphson algorithm.

The structures that appear in the vicinity of the onset and that we investigate here are the following:

(1) Rolls that form a two-dimensional pattern; i.e., they do depend on only one lateral coordinate and are constant along the other. Details about rolls and their stability have been discussed in Ref. [6].

(2) Squares that are mirror-symmetric with respect to the diagonals in the $x$-$y$ plane. Squares may be thought of as two perpendicular sets of rolls with equal amplitudes.

(3) Crossrolls that are not mirror-symmetric to the diagonals in the $x$-$y$ plane. Crossrolls may be thought as two perpendicular sets of rolls with different amplitudes.

Each of these structures can be observed in experiments only for parameters for which they are stable. In order to find the stability regions of the above structures, we applied a restricted stability analysis using the perturbation ansatz

$$\delta X(x,y,z,t) = \sum_{l=-N_l}^{N_l} \sum_{m=-N_m}^{N_m} \sum_{n=-N_n}^{N_n} \delta X_{lmn} e^{st+i[lkx+mky]} f_n(z). \tag{2.14}$$

Here $f_n(z)$, $N_l$, $N_m$, and $N_n$ agree with the definitions above. The restriction to perturbations with the same lateral wavelength as the convection pattern under consideration is necessary because the computational costs of a full stability analysis for perturbations with arbitrary lateral wave numbers would be too high.

Furthermore, the computational effort can be lowered because the perturbations can be divided into certain subclasses:

(1) Perturbations with or without sign change under the mirror-glide operation.

(2) Perturbations that are even in $x$ and $y$, or odd in $x$ and $y$, or even in $x$ and odd in $y$ (or equivalently vice versa).

(3) Perturbations that are symmetric or antisymmetric under change of $x$ and $y$.

The last classification can be applied only to perturbations that fulfill the same symmetries in $x$ and $y$ and only for the stability analysis of squares because crossroll structures are neither symmetric nor antisymmetric under this operation. See Ref. [11] for further details on symmetries and numerical methods.

## III. PROPERTIES OF THE STATIONARY CONVECTIVE STATES

### A. Bifurcation scenarios

For the clear fluid case, the bifurcation scenario of stationary rolls, crossrolls, and squares at positive separation ratios is well known; see, for example, Refs. [10,11]. For porous media we found qualitatively the same scenario, as Fig. 1 shows. There the leading amplitudes are plotted versus the Rayleigh-Darcy number $R$.

The leading amplitude of the velocity potential of rolls, $\Phi_R = \Phi_{101}$, is denoted by the dashed line. The corresponding amplitude of the vertical velocity field is $w_{101} = k^2\Phi_{101}$. When the thermal driving exceeds a critical value $R_c$, $\Phi_R$ becomes positive indicating the onset of roll convection. For the chosen parameters $\psi = 0.4$, $L = 0.1$, and $k = \pi$, we find $R_c \approx 4.8$. This is small compared to the critical Rayleigh-Darcy number $R_c^0 = 4\pi^2$ of a pure fluid. The latter fact is typical for binary mixtures with positive separation ratio and small Lewis number: Due to the positive Soret coupling, the lighter component is driven to the lower plate, which gives rise to a pronounced density difference between the plates. In particular, for small Lewis numbers, where concentration perturbations are barely attenuated, this density difference yields a low convective threshold. Above the onset,

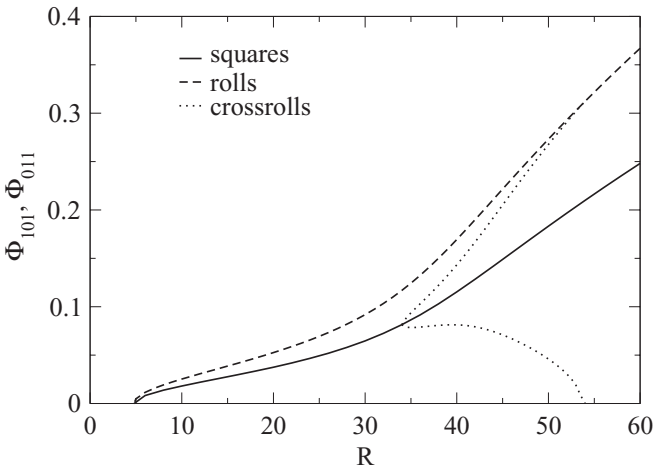


FIG. 1. Bifurcation diagram of rolls (dashed line), squares (solid line), and crossrolls (dotted lines) for $L = 0.1$, $\psi = 0.4$, $k = \pi$. The leading amplitudes of the velocity potential $\Phi$ entering into the representation (2.7) of the velocity field are plotted versus the Rayleigh-Darcy number $R$. The corresponding amplitudes of the vertical velocity are $w_{101} = 2k^2\Phi_{101}$ and $w_{011} = 2k^2\Phi_{011}$ for squares as well as crossrolls and $w_{101} = k^2\Phi_{101}$ for rolls with axes in the $y$ direction.

$\Phi_R$ increases monotonically with $R$ since convection grows with increasing thermal driving.

The leading amplitude of squares is represented by $\Phi_{101}$ or equivalently by $\Phi_{011}$, which are denoted by the solid line in Fig. 1. Square convection can be thought as a nonlinear superposition of two perpendicular roll structures. Due to the square symmetry, both have the same convection strength so that we define $\Phi_S = \Phi_{101} = \Phi_{011}$. Squares emerge at the same critical $R$ as rolls. The leading amplitudes of rolls and squares are approximately connected via the relation $\Phi_R/\Phi_S \approx \sqrt{2}$. In other words, $\Phi_{101}^2 + \Phi_{011}^2$ is approximately the same for both structures. For small thermal driving in the so-called Soret regime, this relation holds true almost exactly, while the ratio increases slightly with growing $R$.

The roll and the square branches are connected by the crossroll branch that exists in a finite $R$-interval. Crossrolls can be interpreted as a superposition of two perpendicular roll sets with different amplitudes. The corresponding leading amplitudes of the two roll sets contributing to the crossrolls are given by $\Phi_{110}$ and $\Phi_{101}$. They are denoted by the dotted lines in our bifurcation diagram. When the thermal driving is increased, crossrolls bifurcate forward out of the square branch above a certain $R$ (here $R \approx 34.05$). Whereas $\Phi_{110}$ is similar to $\Phi_{101}$ near this bifurcation point, one of the amplitudes grows with $R$, while the other decreases until one of the roll sets vanishes and the crossrolls merge into a pure roll state. The orientation of this roll state depends on which of the two symmetry degenerated crossroll states branching off the square state is considered.

We performed also computations to investigate how sensitively our results depend on the model size. They showed that the results in Fig. 1 depend only marginally on the model size $N$: The leading amplitudes that are of relevant size ($|\Phi| \geqslant 0.005$) change less than 0.17% when $N$ is increased from 16 to 20 and less than 0.05% when $N$ is increased from 20 to 24.

For a fixed wave number, the bifurcation scenario described above is valid as long as the Soret effect is sufficiently strong and the concentration diffuses slowly enough. However, the $R$ interval in which crossrolls exist shrinks with decreasing $\psi$ and growing $L$ until crossrolls do not exist anymore. Quantitative results are given in Sec. IV.

### B. Nusselt and mixing numbers

The vertical heat transport in a convective state can be quantified by the Nusselt number

$$\mathrm{Nu} = \frac{\langle j_{\mathrm{tot},z}\rangle_{xy}}{\langle j_{\mathrm{cond},z}\rangle_{xy}}. \tag{3.1}$$

Here $j_{\mathrm{tot},z}$ defines the total vertical heat current density, $j_{\mathrm{cond},z}$ the vertical heat current density in the ground state, and $\langle\cdot\rangle_{xy}$ the lateral average. The Nusselt number can be calculated via the modes obtained by our Galerkin method. Expressed in $\theta$ amplitudes, the Nusselt number at the plates is given by

$$\mathrm{Nu} = 1 - \frac{2\sqrt{2}\pi}{R}\sum_{n=1}^{N}(-1)^n n\theta_{002n}, \tag{3.2}$$

where $N$ denotes the truncation parameter of our Galerkin expansion. Note that for stationary structures like rolls, squares, and crossrolls, the Nusselt number (3.1) is independent of the vertical position. Evaluating the Nusselt number at the plates has the advantage that only $\theta$ amplitudes are needed for the computation. If one calculated Nu at $z \neq \pm\frac{1}{2}$ instead, $\Phi$ amplitudes would enter into Eq. (3.2).

The degree of mixing of the binary fluid is another interesting quantity of the system under consideration. The mixing can be described in terms of the mixing number

$$M = \frac{\sqrt{\langle C^2\rangle - \langle C\rangle^2}}{\sqrt{\langle C_{\mathrm{cond}}^2\rangle - \langle C_{\mathrm{cond}}\rangle^2}}, \tag{3.3}$$

which is defined by the normalized variance of the concentration field. Here $\langle\cdot\rangle$ denotes the total spatial average and $C_{\mathrm{cond}}$ is the concentration field in the ground state.

For roll convection of binary mixtures Nu and $M$ have already been calculated [6]. We refer to this work for a general discussion of the dependence of Nu and $M$ on $\psi$ and $L$ in the case of rolls. Here we focus on a comparison of roll, square, and crossroll convection. Thereto, Fig. 2 shows Nu and $M$ of rolls and squares plotted versus $R$. We fix $L = 0.5, k = \pi$, and investigate different $\psi$ as denoted in the plot.

Close to the onset of convection, Nu and $M$ of squares appear to be almost equal to the respective quantities of rolls. Nu is slightly larger than 1 thus indicating weak advective heat transport. The mixing number takes a value slightly smaller than 1. This illustrates that convection is too weak to equilibrate significantly the concentration gradients caused by the Soret effect. As convection becomes stronger with larger thermal driving, Nu increases and $M$ decreases with $R$. Thereby, the Nusselt number of rolls grows faster than the one of squares. Moreover, while rolls mix both components better for smaller $R$, squares do that when the thermal driving becomes sufficiently strong (see, for example, $\psi = 0.4$ above $R \approx 50$). When the separation ratio of the mixture becomes

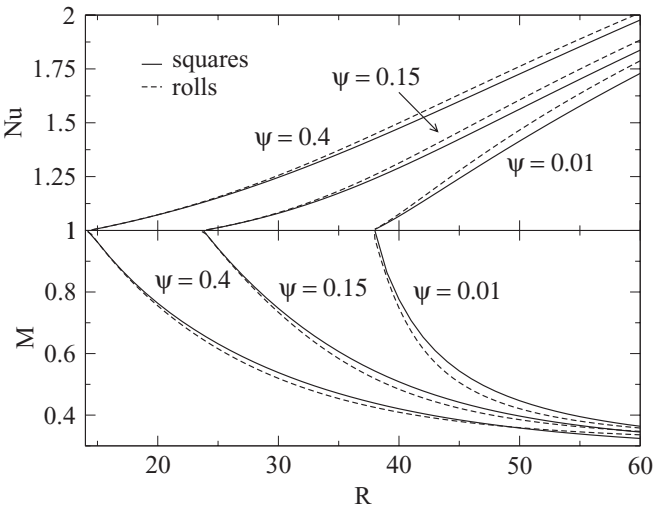


FIG. 2. Nusselt number Nu (top) and mixing number $M$ (bottom) of rolls (dashed lines) and of squares (solid lines) versus $R$ for several $\psi$ as indicated. The other parameters are $L = 0.5$ and $k = \pi$.

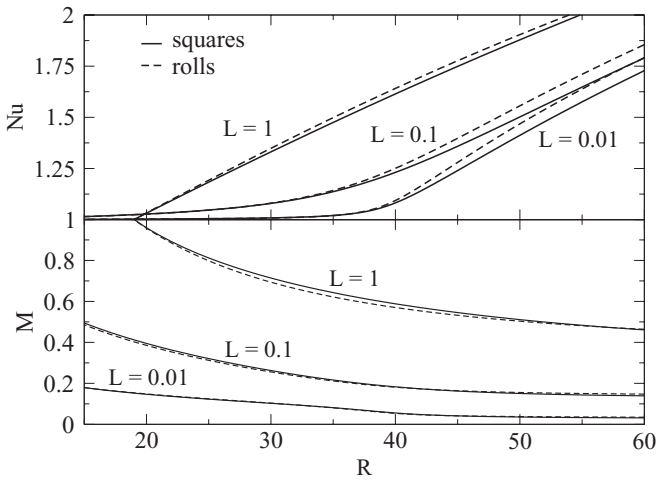


FIG. 3. Nusselt number Nu (top) and mixing number $M$ (bottom) of rolls (dashed lines) and of squares (solid lines) versus $R$ for several $L$ as indicated. The other parameters are $\psi = 0.4$ and $k = \pi$.

larger, the differences between rolls and squares described above decrease.

Figure 3 shows the same as Fig. 2 but for various Lewis numbers and a fixed separation ratio $\psi = 0.4$. Nusselt and mixing numbers of rolls and squares are related in the same way as aforementioned: While Nu and $M$ of rolls and squares are almost equal close to onset, roll convection entails the stronger advective heat transport and square convection the better mixing when $R$ becomes large enough. The difference in Nu grows with smaller $L$ whereas the difference in $M$ decreases. Exemplarily, we tested the influence of the model size $N$ on Nu for the parameter combination $L = 0.1$ and $\psi = 0.4$. We found that the Nusselt number changes less than 0.0001% when $N$ is decreased from 24 to 16.

For the sake of clarity, we have not included so far Nusselt and mixing numbers for the crossroll state. Nu and $M$ for crossrolls are plotted in Fig. 4 for the parameters $\psi = 0.4$, $L = 0.01$, and $k = \pi$ in a slightly more narrow $R$-range than

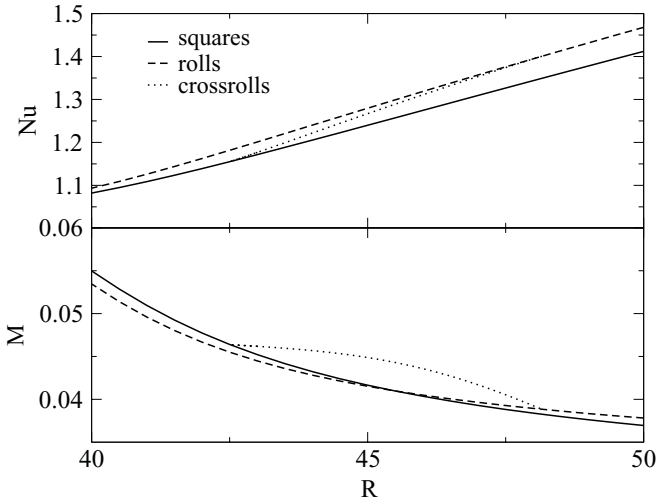


FIG. 4. Nusselt number Nu (top) and mixing number $M$ (bottom) of crossrolls (dotted lines), rolls (dashed lines), and squares (solid lines) versus $R$. Parameters are $L = 0.01$, $\psi = 0.4$, $k = \pi$.

in Figs. 2 and 3. The Nusselt number of crossrolls lies for all $R$ above the one of squares and below the one of rolls. Moreover, crossroll convection always causes a weaker mixing than roll and square convection. For other parameter combinations of $L$ and $\psi$, we have found a similar picture except for the fact that the mixing of crossrolls can be better than the one of squares in a small $R$ interval close to the point where crossrolls merge into rolls. The latter scenario can be observed for smaller $\psi$, for instance, $\psi = 0.15$ and $L = 0.01$.

### C. Structure of the fields

The temperature and the concentration fields of squares as well as the isolines of the $z$ component $w$ of their velocity field are shown in Fig. 5. The fields and $w$ isolines are displayed for the lateral cross section of one convection cell at midheight, i.e., $z = 0$ for the parameters $L = 0.01$, $\psi = 0.3$, and $k = \pi$. We investigate two different strengths of thermal driving, $R = 20$ and 40. The $w$ isolines illustrate how the fluid is interchanged between both plates: The fluid is convected from the lower to the upper plate across the corners of the cross section depicted. Then, the fluid streams near the upper plate to the middle of the depicted area and flows down to the lower plate again.

Another interesting feature of the $w$ isolines is their deformed, complex shape for $R = 20$ as typical for small $L$ in the so-called Soret regime, where convection is mainly due to the destabilizing Soret effect. These deformations can be explained in analogy to the deformations of the streamlines of rolls [6]: In the Soret regime, buoyancy is mainly caused by the very anharmonic concentration field. Via the buoyancy term in the momentum balance, this anharmonicity is imposed onto the velocity field, too. This becomes apparent in our

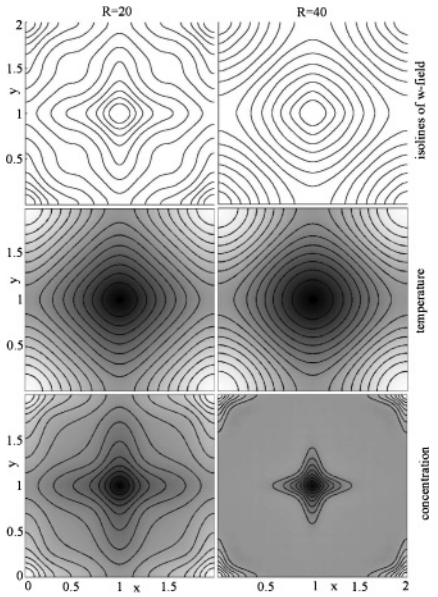


FIG. 5. Structure of square convection in a horizontal cross section at midheight, $z = 0$, covering one wavelength. Shown are isolines of $w$ (top) and gray-scale representations with isolines of temperature (middle) and concentration (bottom). Parameters are $R = 20$ (left column) and $R = 40$ (right column). Furthermore, $L = 0.01$, $\psi = 0.3$, $k = \pi$.

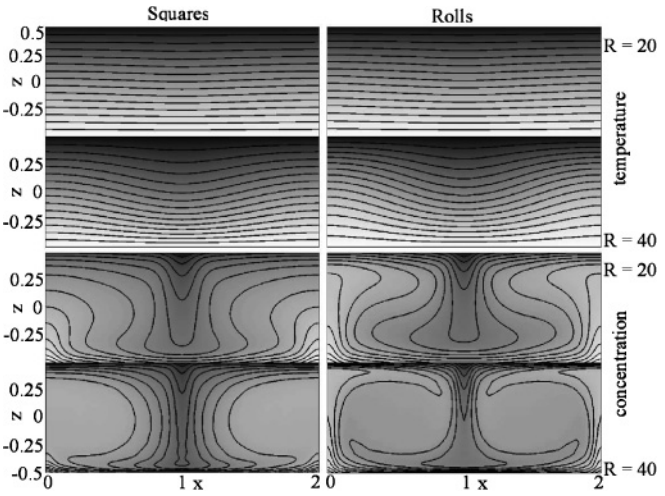


FIG. 6. Structure of square and roll convection in a vertical cross section covering one wavelength. Shown are gray-scale representations with isolines of temperature and of concentration in squares at $y = 1$ (left column) and in rolls (right column). Parameters are $R = 20$ (top stripe) and $R = 40$ (bottom stripe) of each subgraph. Furthermore, $L = 0.01$, $\psi = 0.3$, $k = \pi$.

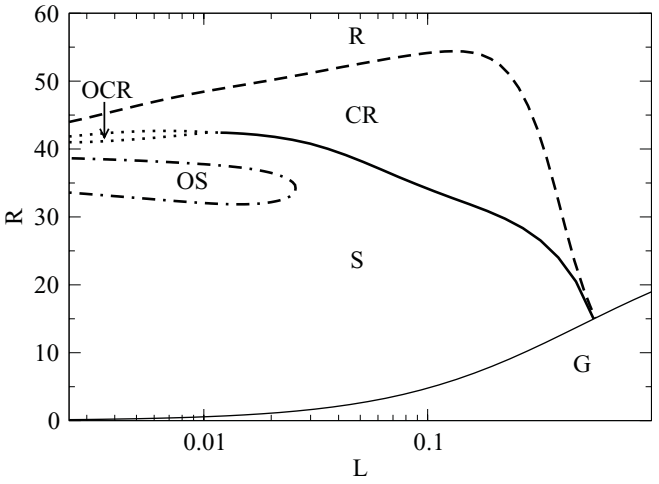


FIG. 7. Phase diagram for $\psi = 0.4$, $k = \pi$, and $\phi^* = 1$. In the regimes denoted by G, R, S, and CR, the ground state, rolls, squares and crossrolls are stable, respectively. In the area marked by OS, squares are destabilized by oscillatory perturbations with square symmetry; in the area marked by OCR, we expect oscillatory crossrolls.

plot: The $w$ isolines coincide almost exactly with the isolines of the concentration field. Since we model the transport of momentum on the basis of Darcy's law (2.1b), there is no diffusion which would smooth out the deformation. On the other hand, in the clear fluid case, the relaxation term $-\boldsymbol{u}$ is replaced by the momentum diffusion term $\Delta\boldsymbol{u}$, and the velocity field is generally much smoother in the Soret regime.

When the thermal driving is increased, the buoyancy is generated more and more by the smoother temperature field, whereas the influence of the concentration field on the buoyancy becomes negligible. For $R = 40$, the $w$ isolines agree already very well with the isolines of the temperature field.

Figure 6 shows additionally the temperature and concentration fields of squares for one periodicity interval in the vertical cross section at $y = 1$. The parameters are chosen as in Fig. 5, and we have included the respective fields of rolls for comparison. The temperature fields of both structures can barely be distinguished in the cross section depicted; for $R = 20$, the convection is weak such that advection changes the linear temperature profile of the ground state only slightly. For $R = 40$, the thermal driving has become strong enough to modulate the temperature visibly.

The differences between rolls and squares become more obvious in the concentration field. Squares show a broader concentration boundary layer than rolls in the down-flow regime around $x = 1$. At the margins of the depicted cross section, rolls show a corresponding up-flow. This does not hold for squares where the up-flow is found at $(x, y) = (0,0)$ (see Fig. 5).

## IV. STABILITY OF SQUARES AND CROSSROLLS

For our system, the stability of rolls has been investigated for pure fluids [1,2] as well as for binary mixtures [6]. In this section we will extend this work by carrying out a restricted stability analysis for squares and crossrolls. The analysis is restricted in so far that only perturbations are taken into account that have the same lateral periodicity as the underlying pattern.

### A. Phase diagrams

Figure 7 gives an overview over the stability regimes of the different structures and the corresponding stability boundaries in the $L$-$R$ plane. We choose $\psi = 0.4$ and with $k = \pi$ a medium wave number. Because we take time-dependent instability mechanisms into account, we have to specify the value of the normalized porosity. We choose $\phi^* = 1$ in Fig. 7. Inside the regimes marked with R, S, or CR in our phase diagram, stationary rolls, squares, or crossrolls are stable. Neither of these structures are stable in the regimes denoted by oscillatory crossrolls (OCRs) or oscillatory squares (OSs).

For $R$ values above the thin solid line in Fig. 7, the ground state becomes unstable against stationary perturbations with the lateral wave number $k = \pi$. The resulting pattern is a roll state when the Lewis number is larger than $L \approx 0.55$ where the dashed line branches from the thin line representing the stability boundary of the ground state. Below the dashed line, rolls become unstable against stationary perturbations and are replaced by crossrolls. In the corresponding bifurcation diagram, this transition belongs to the point where the crossroll branch merges into the roll branch (compare with Fig. 1 for $L = 0.1$). Since crossrolls are even in the $x$ as well as in the $y$ direction and since they have the same periodicity in both directions, the same symmetries are found for the perturbations that trigger the replacement of rolls by crossrolls. However, we mention that the dashed line does not correspond to a point on the CR boundary computed in Ref. [6]. The reason is that here the perturbations are restricted to be periodic in the $x$ and $y$ direction with periodicity interval $\frac{2\pi}{k}$, while this restriction is not imposed in the analysis of Ref. [6]. Thus, a comparison of these two results shows that the stabiliy domain of rolls is

smaller than shown in Fig. 7—unrestricted CR perturbations destabilize rolls already above the dashed line in Fig. 7.

For $L < 0.55$, rolls become unstable at the onset giving rise to stable squares. The stability regimes of squares above onset is restricted by three different stability boundaries. The first one, denoted by the thick solid line, is related to stationary perturbations which tend to replace squares by crossrolls when the thermal driving becomes strong enough. This transition occurs at the Rayleigh-Darcy number where the crossroll branch bifurcates forward out of the square branch; see the bifurcation diagram in Fig. 1 for $L = 0.1$. The perturbations related to this transition are even in the $x$ and $y$ directions and have the same periodicity in both directions for the same reason as stated above. Since squares are symmetric under reflection at the lateral main diagonal but crossrolls are not, the perturbations have to break this symmetry; i.e., they are antisymmetric under this reflection.

The second stability boundary of squares is illustrated by the lower dotted line in Fig. 7. It occurs at small $L$ only (here for $L < 0.015$), where it precedes the stability boundary described above. The corresponding perturbations have the same symmetries as the stationary perturbations, which tend to replace squares by crossrolls, but here they are oscillatory. We suppose that the perturbations give rise to the growth of the so-called oscillatory crossrolls (OCRs) because perturbations of the same type lead to the OCR structure in the clear fluid case [9,10,17]. However, in the system with a porous medium, the simulation of oscillatory crossrolls seems to require that higher modes are considered in the ansatz for the Galerkin method than for the clear fluid, i.e., $N > 16$ instead of $N = 12$. So we could not verify the existence of nonlinear OCR solutions in the porous medium.

The third stability boundary of squares, given by the dash-dotted line, destabilizes squares in the area denoted by oscillatory squares (OSs) in Fig. 7. The instability is generated by perturbations that are oscillatory but have the same spatial symmetries as the square pattern itself. Therefore, we call it OS instability. The OS instability has no analog in the clear fluid case. An explicit time integration showed chaotic behavior in the OS area, but we cannot rule out that regular convection patterns are found there if one uses larger Galerkin models, say, with $N > 16$.

For crossrolls, we detected only one relevant instability mechanism displayed by the upper dotted line in Fig. 7. By contrast, the dashed and the thick solid lines, which mainly restrict the regime of crossrolls, are not stability boundaries for crossrolls but indicate the finite $R$-interval in which the crossroll state exists: Above the dashed line crossrolls merge into rolls and below the thick solid line into squares. The instability related to the dotted line occurs for small $L$ (here for $L < 0.015$) when the thermal driving becomes weak enough. This mechanism should replace crossrolls by OCRs, which we expect to exist in the small area denoted by OCRs. The corresponding perturbations are oscillatory and show the same spatial symmetries as crossrolls and OCRs.

#### 1. Model size dependence

Further computations have been carried out to investigate the influence of the model size $N$ on the results in Fig. 7. When we increase $N$ from 16 to 28 (or from 24 to 28), the $R$ position of the dashed line changes less than 3.7% (0.73%) for a given $L$, the $R$ position of the solid as well as upper dotted line less than 2.8% (0.70%), and the $R$ position of the dash-dotted line less than 2.4% (0.2%).

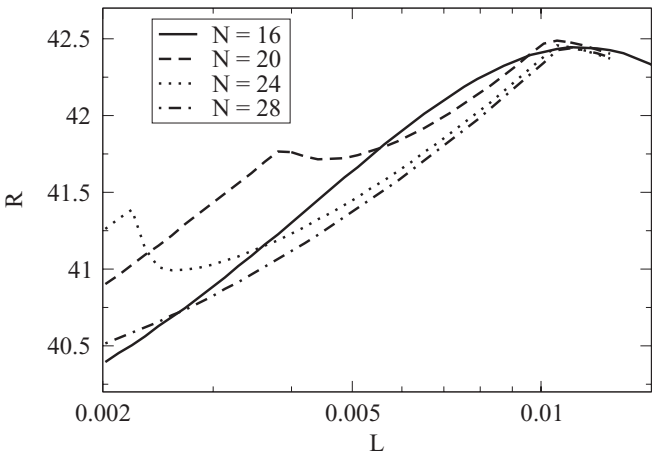


FIG. 8. Model size dependence of the boundary above which squares become unstable against perturbations of crossroll symmetry. The lines refer to model sizes ranging from $N = 16$ to 28 as indicated in the legend. Parameters are $\psi = 0.4$, $k = \pi$, and $\phi^* = 1$.

The convergence of the lower dotted line is investigated in Fig. 8 that depicts the boundary above which squares become unstable against perturbations of crossroll symmetry. For $N = 16$, the perturbations are stationary for all $L$, and OCRs do not exist. For $N = 20$, the perturbations are oscillatory from $L \approx 0.004$ to $L \approx 0.01$, for $N = 24$, from $L \approx 0.0023$ to $L \approx 0.01$ and, for $N = 28$, from an $L < 0.002$ to $L \approx 0.011$. For $L \geqslant 0.005$, the OCR boundary has almost converged for $N = 28$, while, for smaller $L$, a larger model size might be needed to get close to the real position of the OCR boundary.

#### 2. OCR, crossroll, and square patterns

When the normalized porosity differs from $\phi^* = 1$, only the oscillatory stability boundaries are changed, i.e., the boundaries that limit the OCR and the OS regimes in Fig. 7. In Fig. 9 we investigate the OCR regime. Here the model size is chosen to be $N = 28$ to account for the strong model dependence of the OCR boundary. According to Fig. 9, the OCR regime shrinks with $\phi^*$ and disappears at the latest when the normalized porosity reaches the value 0.5. For $\phi^* \leqslant 0.5$, the regime of stable squares is bounded toward larger $R$ by the solid line in Fig. 9 above which squares are replaced by crossrolls. This boundary remains the same for all $\phi^*$ but is preceded by the oscillatory boundary in a certain $L$ range for large enough $\phi^*$, in our phase diagram of Fig. 7, for example, below $L \lessapprox 0.015$.

The positions of the stability boundaries in Fig. 9 are derived from the behavior of the most critical eigenvalues. Figure 10 shows the real parts of the two most critical eigenvalues versus $R$ for $\psi = 0.4$, $L = 0.004$, and $k = \pi$ to illustrate the connection between crossrolls and OCRs. The underlying pattern is a square state and the perturbations have crossroll symmetry. We compare the eigenvalues for two different normalized porosities, $\phi^* = 1$ and 0.5. Both of these

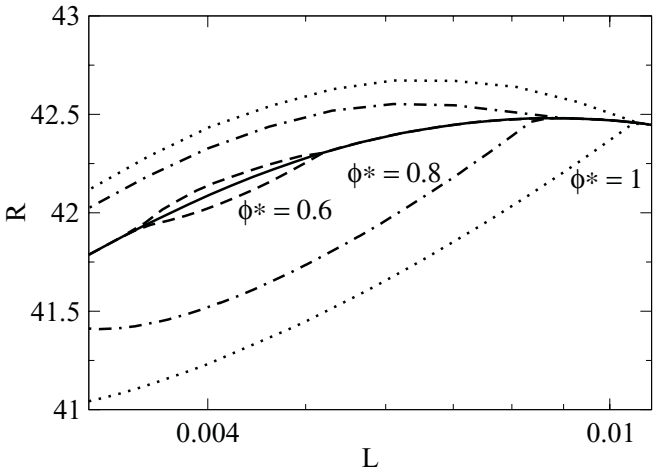


FIG. 9. Regimes in which oscillating crossrolls can be expected for different porosities $\phi^*$. OCR perturbations grow at the dotted lines if $\phi^* = 1$, at the dash-dotted lines if $\phi^* = 0.8$, and at the dashed lines if $\phi^* = 0.6$. The upper (lower) lines mark the bifurcation thresholds of OCR solutions out of the stationary crossroll (square) state. At $\phi^* = 0.5$ the OCR regime has shrunk to zero. The solid line denotes the threshold for the forwards bifurcation of stationary crossrolls (toward larger $R$) out of the square solution. This threshold does not depend on $\phi^*$. Parameters are $L = 0.01$, $\psi = 0.4$, $k = \pi$. Considering the slow convergence of the OCR perturbations, the model size is chosen to $N = 28$ in the figure.

eigenvalues have a negative real part. Thus, squares are stable at $R = 40$ in either case.

For $\phi^* = 1$, squares remain stable until the real part of the complex conjugated pair passes through 0 at $R \approx 41.25$ and becomes positive. Here squares are destabilized against the oscillatory perturbations that we expect to establish the OCR state. For $\phi^* = 0.5$, on the contrary, the pair does not pass through 0 but splits up into two real eigenvalues at $R \approx 42.06$. While one of them becomes smaller, the other becomes larger

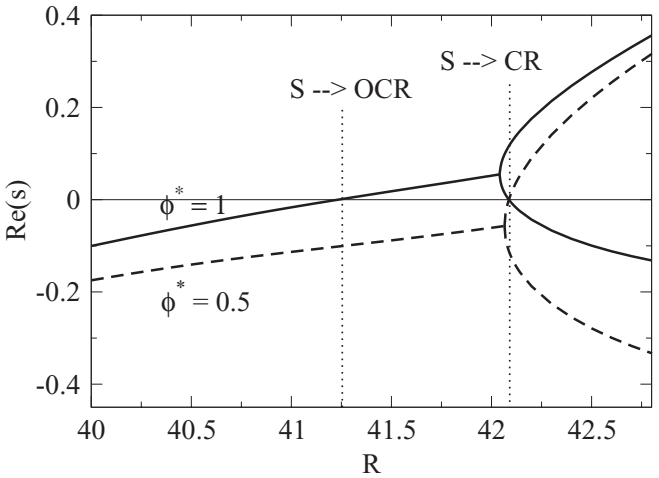


FIG. 10. Stability analysis of squares: real parts of the relevant eigenvalues plotted versus $R$. Vertical dotted lines identify the $R$-values for the loss of stability to OCR and to CR perturbations, i.e., the corresponding bifurcation thresholds. Solid lines refer to $\phi^* = 1$ and dashed lines to $\phi^* = 0.5$. Parameters are $\psi = 0.4$, $L = 0.004$, $k = \pi$.

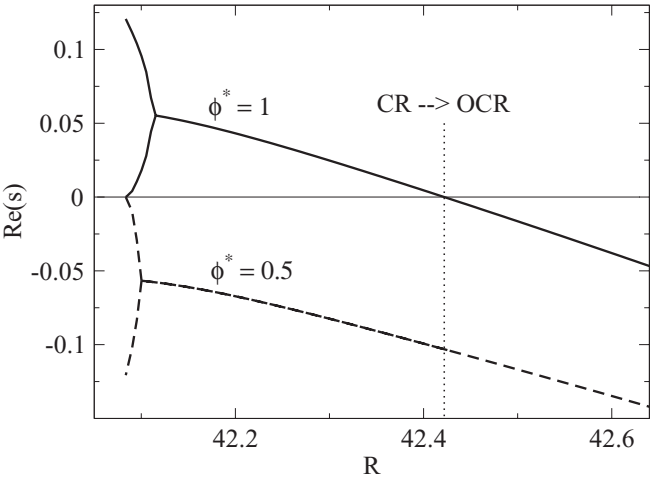


FIG. 11. Stability analysis of crossrolls: real parts of the relevant eigenvalues plotted versus $R$. Vertical dotted line identifies the $R$-value for the loss of stability to an OCR perturbation, i.e., the corresponding bifurcation threshold. Solid line refers to $\phi^* = 1$ and dashed line to $\phi^* = 0.5$, respectively. Parameters are $\psi = 0.4$, $L = 0.004$, $k = \pi$.

and crosses the zero axis at $R \approx 42.08$. At this value, squares are destabilized by the stationary perturbations that tend to establish crossrolls. After the complex conjugated pair has split up in the case $\phi^* = 1$, the real part of the second greatest eigenvalue crosses through 0 from above at $R \approx 42.08$. Thus, there is a zero crossing at the same $R$ for both normalized porosities indicating the point where crossrolls bifurcate out of squares. Consequently, this bifurcation point is independent of $\phi^*$ as expected.

Figure 11 shows the relevant eigenvalues for crossrolls as underlying pattern. Except for a different $R$ range, the parameters are the same as in the Fig. 10. Exactly at the bifurcation point $R \approx 42.08$, where the crossroll branch connects to the square branch, the eigenvalues are equal to those related to the square pattern discussed above. For larger $R$, however, the eigenvalues behave differently. For squares, there is at least one positive eigenvalue indicating that squares are always unstable above the bifurcation point; see Fig. 10. For crossrolls, on the contrary, all eigenvalues become negative when the thermal driving is sufficiently strong. This occurs either at the bifurcation point itself as for $\phi^* = 0.5$ where oscillatory instabilities play no role, or otherwise for larger $R$, for example, at $R \approx 42.42$ for $\phi^* = 1$. In the second case, the zero crossing determines the upper limit of the OCR regime. Before this zero crossing, the two most critical values have formed a complex conjugated pair indicating, that the corresponding instability is an oscillatory one.

### B. The oscillating square instability

In this section we discuss the parameter dependence of the OS regime in which squares are destabilized by oscillatory perturbations with square symmetry. The wave number of the square state remains fixed to $k = \pi$. In Fig. 12 we choose $L = 0.01$ and $\psi = 0.1$ and show with the dash-dotted lines the boundaries of OS regime versus $\phi^*$. As one can see, the OS regime is shifted slightly toward smaller $R$ when $\phi^*$ is

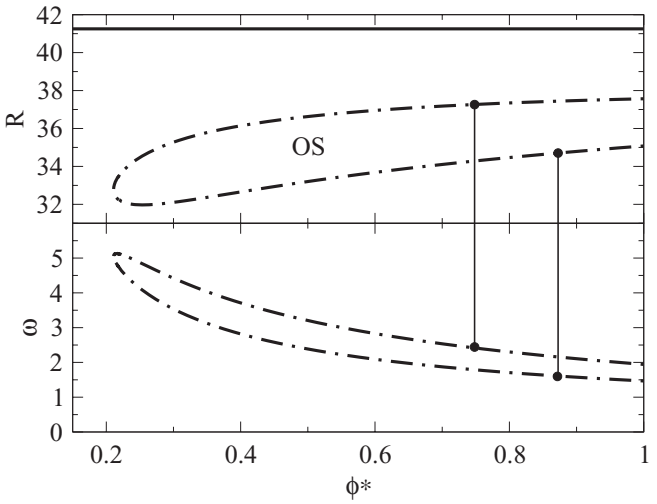


FIG. 12. Bifurcation properties of oscillating squares versus $\phi^*$. Dash-dotted lines show the bifurcation thresholds of OS convection out of stationary squares (top figure) and the oscillation frequencies (bottom figure) at threshold. Vertical lines identify their relation. The full line in the top figure is the bifurcation threshold of stationary crossrolls out of square convection. Parameters are $L = 0.01$, $\psi = 0.1, k = \pi$.

decreased. When the normalized porosity becomes too small the OS area shrinks and finally disappears below $\phi^* \approx 0.21$. In other words, the oscillatory perturbations loose their influence for small $\phi^*$, i.e., when the influence of the porous medium becomes strong. The same tendency has already been observed in the last section for the OCR instability as well as in Ref. [18] for the oscillatory perturbations that destabilize the ground state at $\psi < 0$ and in Ref. [6] for the oscillatory perturbations that destabilize rolls for small $L$.

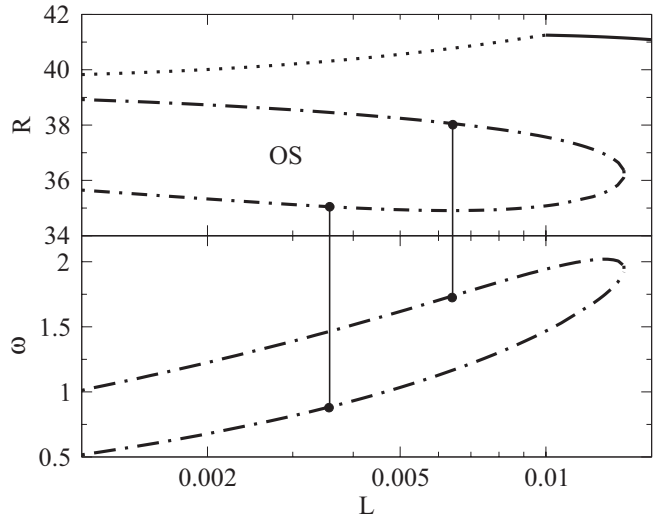


FIG. 13. Bifurcation properties of oscillating squares versus $L$. Dash-dotted lines show the bifurcation thresholds of OS convection out of stationary squares (top figure) and the oscillation frequencies (bottom figure) at threshold. Vertical lines identify their relation. The full line in the top figure is the bifurcation threshold of stationary crossrolls out of square convection and the dotted line the one to OCRs. Parameters are $\psi = 0.1, \phi^* = 1, k = \pi$.

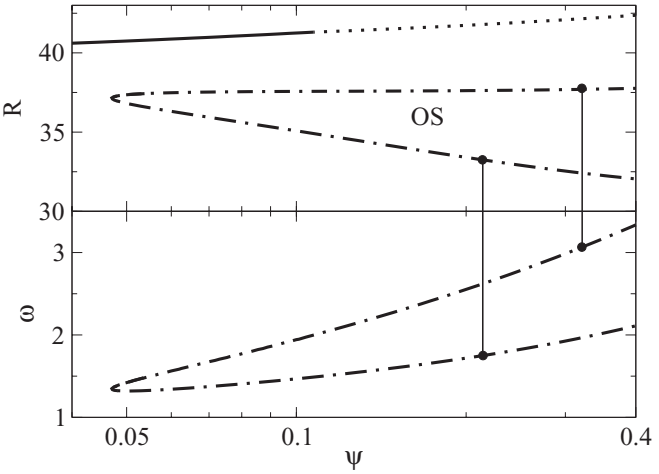


FIG. 14. Bifurcation properties of oscillating squares versus $\psi$. Dash-dotted lines show the bifurcation thresholds of OS convection out of stationary squares (top figure) and the oscillation frequencies (bottom figure) at threshold. Vertical lines identify their relation. The full line in the top figure is the bifurcation threshold of stationary crossrolls out of square convection and the dotted line the one to OCRs. Parameters are $L = 0.01, \phi^* = 1, k = \pi$.

The onset frequencies $\omega$ at the boundaries of the OS regime are included in the lower part of Fig. 12. $\omega$ is obtained in our stability analysis as the imaginary part of the most critical eigenvalue. As indicated by the vertical lines, the branch with the higher frequency belongs to the branch at higher $R$. When $\phi^*$ decreases, the frequencies of both branches grow until the OS regime disappears.

The dependence of the OS regime on the Lewis number $L$ is investigated in Fig. 13. We choose again $\psi = 0.1$, and $\phi^* = 1$. With increasing $L$, the OS regime is shifted slightly toward smaller $R$ and vanishes above $L \approx 0.0145$. The frequencies grow with $L$.

Finally, the dependence of the OS bifurcation threshold on the separation ratio $\psi$ is analyzed for $L = 0.01$ and $\phi^* = 1$ in Fig. 14. While the upper branch of the OS threshold depends barely on $\psi$, the lower branch is moved to greater $R$ when $\psi$ decreases such that the OS regime disappears below $\psi \approx 0.047$. The frequencies become smaller with decreasing $\psi$.

Summarizing, the OS regime shrinks when $\phi^*$ or $L$ is increased or when $\psi$ is decreased. The frequency of the instability grows when $\phi^*$ or $\psi$ becomes smaller or when $L$ becomes larger.

### C. Stability analysis in the $k$-$R$ plane

So far, we have investigated only the stability of patterns with lateral wave number $k = \pi$. The wave-number dependence of the stability boundaries is depicted in Fig. 15 where the $k$-$R$ plane is shown for $\phi^* = 1$ and several $L$-$\psi$ combinations. The stability boundaries are denoted by the same line types as in our phase diagram in Fig. 7 apart from one exception: Although the thick solid line indicates further on the location where squares are destabilized by stationary perturbation with crossroll symmetry, we have not tested whether squares are replaced by crossrolls when this boundary is traversed at the small-$k$ side where the thick solid line kinks downward.

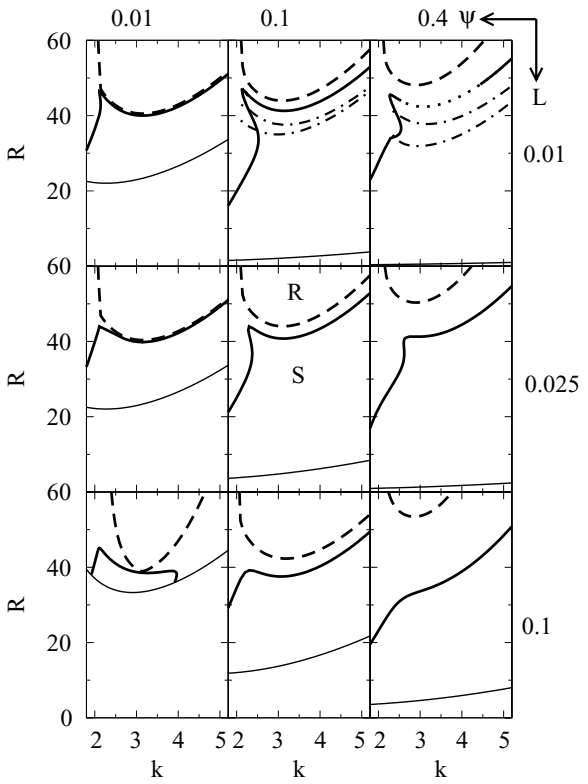


FIG. 15. Stability boundaries in the $k$-$R$ plane for $\phi^* = 1$ and several $L - \psi$ combinations. The line style is as in Fig. 7: The ground state is stable below the thin lines denoting the bifurcation threshold of squares, at the full lines stationary crossrolls bifurcate out of the square solution branch; the dotted line identifies the narrow $R$-interval where OCR perturbations can grow, the dash-dotted lines are bifurcation thresholds of oscillating squares, and roll convection becomes stable above the dashed lines.

Figure 15 can be compared to the phase diagram of Fig. 7, for example, by means of the plot for the parameter combination $\psi = 0.4$ and $L = 0.01$. When moving in this plot upward in $R$ at fixed $k = \pi$ we recognize the sequence of the convection structures in the phase diagram of Fig. 7: When the thermal driving increases, the ground state becomes unstable against squares above the thin solid line. Then squares are destabilized by the OS perturbations above the lower dash-dotted line until they become stable again beyond the upper dash-dotted line. When $R$ grows above the dotted line, squares are presumably replaced by OCRs, which in turn are replaced by stationary crossrolls for slightly higher Rayleigh-Darcy numbers. Note that only the lower boundary of the OCR regime is displayed in the plot since the upper one lies very close ($\Delta R < 0.25$) and thus cannot be resolved sufficiently. Finally, stationary crossrolls are transformed into rolls beyond the dashed line. According to Fig. 15, this sequence of structures remains unchanged for a wide range of wave numbers, i.e., $2.55 \leqslant k \leqslant 4.44$. For wave numbers outside this range, however, the OCR regime vanishes. Moreover, the thick solid line kinks downward and the dashed line kinks upward at the small-$k$ side, thus leaving a regime that we have not tested for convection patterns.

In addition, the plot for $\psi = 0.4$ and $L = 0.01$ shows the following: When the wave number changes from $k = \pi$ to larger $k$, the onset of convection and with it the stability regime of rolls, squares, and crossrolls as well as the OS regime are shifted toward higher $R$. The $R$-interval in which crossrolls are stable increases slightly with $k$, whereas the OS regime shrinks. According to the other plots in Fig. 15, these changes with $k$ hold true for a wide range of $\psi$-$L$ combinations. Also, the sequence of the stability boundaries for intermediate wave numbers remains the same for the other parameter combinations depicted except for the following facts: The OCR regime disappears for all other parameter combinations in Fig. 15. Hence, we conclude that the OCR regime shrinks when $\psi$ becomes smaller or when $L$ becomes larger—its $L$ dependence has already been deduced from the phase diagram in Fig. 7. Furthermore, as well, the OS regimes emerges only in the plot for $\psi = 0.1$ and $L = 0.01$. This is consistent with our findings in Sec. IV B that the OS regime shrinks when $L$ grows or when $\psi$ is decreased.

With Fig. 15, we can additionally discuss the dependence of the stability regimes of squares and crossrolls on the separation ratio. When $\psi$ is increased, i.e., when the Soret coupling becomes stronger, both stability regimes expand. In other words, a strong Soret effect allows for three-dimensional patterns to exist in a large $R$-interval. This important result is not restricted to porous media, but it is valid in the clear fluid case as well [11]. The plot for the parameter combination $\psi = 0.01$ and $L = 0.1$ represents a case where square convection is restricted to a finite, relatively small $R$-$k$ domain since the Soret coupling is weak.

When the separation ratio $\psi$ falls below a certain value, which depends on $L$, the $R$-$k$ regime of squares shrinks, and squares do no longer exist as a stable convection pattern. Then crossrolls transferring the stability from squares to rolls no longer exist as well.

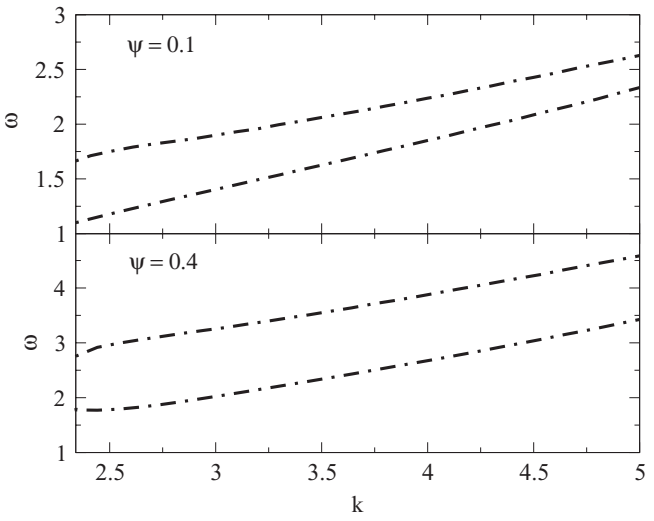


FIG. 16. Wave-number dependence of the frequencies of oscillating squares for $\psi = 0.1$ and 0.4. Lines show the frequencies at the OS bifurcation thresholds that are marked in Fig. 15 by dash-dotted lines. In each case the upper (lower) frequency branch corresponds to the upper (lower) bifurcation threshold. Parameters are $L = 0.01$, $\phi^* = 1$.

For the sake of completeness, Fig. 16 shows how the frequencies of the OS perturbations in Fig. 15 grow with wave number. The branch with the higher frequency belongs again to the branch at greater $R$. In the $k$-range depicted, the frequencies on both branches increase almost linearly with $k$.

## V. CONCLUSION

In this paper we have investigated roll, crossroll, and square convection of binary mixtures in the Rayleigh-Bénard system with porous medium for positive Soret coupling using a multimode Galerkin method. The bifurcation scenarios of the structures resemble qualitatively to the ones in the clear fluid case: When the Rayleigh-Darcy number $R$ increases, squares and rolls bifurcate simultaneously forward out of the ground state. If the Soret effect is strong enough, the roll and square states are connected via a crossroll branch that bifurcates forward from the square state when $R$ grows.

Additionally to the bifurcation behavior, we carried out a restricted linear stability analysis. The analysis is restricted insofar that only perturbations are considered that have the same lateral periodicity as the underlying structure. According to this analysis, squares are stable above onset for sufficiently small Lewis number $L$ and for sufficiently large separation ratio $\psi$. When $R$ increases, squares are destabilized by perturbations with crossroll symmetry. For large $L$ and large normalized porosities $\phi^*$ as well as for small $\psi$, these perturbations are oscillatory. Otherwise, they are stationary. The stationary perturbations tend to replace squares by crossrolls at the $R$ value where the crossroll branch bifurcates from the square branch. The oscillatory perturbations, on the contrary, are supposed to give rise to an oscillatory crossrolls state below the $R$ value where the crossroll branch bifurcates from the square branch—as has also been observed in the clear fluid case. When $R$ grows further on, the OCR state is replaced by stationary crossrolls. The stationary crossrolls remain stable until they are replaced by rolls at the $R$ value where the crossroll branch connects to the roll branch.

A new instability mechanism was found for which no equivalent is known in the clear fluid case. The corresponding perturbations are oscillatory and have square symmetry, and they destabilize squares in a small $R$ interval. Thus, we called it oscillatory square (OS) instability. In the OS regime where squares are destabilized by the OS perturbations we could not compute a regular convection pattern. Instead, an explicit time integration showed chaotic behavior. However, this apparent absence of a stable OS structure might be caused by too severe a mode truncation in our Galerkin method. The OS regime shrinks until it disappears when the normalized porosity or the Lewis number is increased or when the separation ratio is decreased. Moreover, the frequency of the OS instability grows when $\phi^*$ or $\psi$ becomes smaller or when $L$ becomes larger.

The sequence of stability regimes described above was found for $k = \pi$, and it remains the same over a wide range of lateral wave numbers. When the wave number changes from $k = \pi$ to larger $k$, the onset of convection and the stability regime of rolls, squares, and crossrolls as well as the OS regime are shifted toward higher $R$. The $R$-interval in which crossrolls are stable increases slightly with $k$, whereas the OS regime shrinks. Furthermore, the frequencies of the OS perturbations grow with $k$.

To compare the fixed-point properties of stationary rolls, squares, and crossrolls with each other, we computed their Nusselt number Nu and mixing number $M$ over a large parameter range of $\psi$-$L$ combinations. Close to the onset of convection, Nu and $M$ of rolls are almost equal to the respective quantities of squares. The advective heat transport of rolls grows faster with $R$ than the one of squares when $R$ increases. Moreover, the mixing of the binary fluid grows faster with $R$ for rolls in the Soret regime, while it does so for squares in the Rayleigh regime. The differences in Nu and $M$ decrease when the separation ratio increases. Moreover, when the Lewis number decreases, the difference in Nu becomes larger, whereas the difference in $M$ becomes smaller.

The Nusselt number of crossrolls lies for all $R$ above the one of squares and below the one of rolls. Additionally, crossrolls always mix both components of the fluid weaker except for certain $\psi$-$L$ combinations in a small $R$-interval close to the point where crossrolls merge into rolls.

Finally, we investigated the $w$ isolines of squares and compared their temperature field and concentration field with the respective fields of rolls. Squares showed broader and thus smoother concentration boundary layers than rolls. In the so-called Soret regime where the bouyancy is dominated by concentration gradients the $w$ isolines of squares were found to have a deformed complex shape as a result from an interplay between the Soret effect, advection, and the absence of momentum diffusion.


[1] J. M. Straus, J. Fluid Mech. **64**, 51 (1974).

[2] M. De La Torre Juárez and F. H. Busse, J. Fluid Mech. **292**, 305 (1995).

[3] M. D. Shattuck, R. P. Behringer, G. A. Johnson, and J. G. Georgiadis, J. Fluid Mech. **332**, 215 (1997).

[4] L. E. Howle, R. P. Behringer, and J. G. Georgiadis, J. Fluid Mech. **332**, 247 (1997).

[5] K. Vafai, ed., *Handbook of Porous Media* (Springer-Verlag, New York, 2005).

[6] R. Umla, M. Augustin, B. Huke, and M. Lücke, J. Fluid Mech. **649**, 165 (2010).

[7] M. Augustin, R. Umla, B. Huke, and M. Lücke, Phys. Rev. E **82**, 056303 (2010).

[8] E. Moses and V. Steinberg, Phys. Rev. A **43**, 707 (1991).

[9] M. A. Dominguez-Lerma, G. Ahlers, and D. S. Cannell, Phys. Rev. E **52**, 6159 (1995).

[10] Ch. Jung, B. Huke, and M. Lücke, Phys. Rev. Lett. **81**, 3651 (1998).

[11] B. Huke, M. Lücke, P. Büchel, and C. Jung, J. Fluid Mech. **408**, 121 (2000).

[12] P. Vadasz, Transport in Porous Media **59**, 341 (2005).

[13] D. A. Nield and A. Bejan, eds., *Convection in Porous Media* (Springer-Verlag, New York, 2006).
[14] H. W. Müller and M. Lücke, Phys. Rev. A **38**, 2965 (1988).
[15] B. Huke, H. Pleiner, and M. Lücke, Phys. Rev. E **75**, 036203 (2007).
[16] St. Hollinger and M. Lücke, Phys. Rev. E **57**, 4238 (1998).
[17] P. Le Gal, A. Pocheau, and V. Croquette, Phys. Rev. Lett. **54**, 2501 (1985).
[18] M. Charrier-Mojtabi, B. Elhajjar, and A. Mojtabi, Phys. Fluids **19**, 124104 (2007).